

Effect of ceramic preform geometry on load partitioning in Al_2O_3 –Al composites with three-dimensional periodic architecture

M.L. Young^{a,*}, R. Rao^b, J.D. Almer^c, D.R. Haeffner^c, J.A. Lewis^b, D.C. Dunand^a

^a Department of Materials Science and Engineering, Northwestern University, Evanston, IL 60208, USA

^b Department of Materials Science and Engineering, University of Illinois, Urbana, IL 61801, USA

^c Advanced Photon Source, Argonne National Laboratory, Argonne, IL 60439, USA

ARTICLE INFO

Article history:

Received 1 April 2009

Received in revised form 11 July 2009

Accepted 17 July 2009

Keywords:

Metal matrix composites (MMC)

Synchrotron radiation

X-ray diffraction (XRD)

Aluminum

Compression test

ABSTRACT

Interpenetrating Al_2O_3 /Al composites were created by liquid-metal infiltration of 3D periodic ceramic preforms with face-centered-tetragonal symmetry produced by direct-write assembly. Volume-averaged lattice strains in the ceramic phase of the composite were measured by synchrotron X-ray diffraction for various levels of uniaxial compression stresses. Load transfer is found to occur from the metal phase to the ceramic phase, and the magnitude of the effect is in general agreement with simple rule-of-mixtures models. Spatially resolved diffraction measurements show variations in load transfer at two different positions within the composite for the elastic- and damage-deformation regimes, the latter being observed using phase-enhanced synchrotron imaging. The mechanical behavior of these interpenetrating Al_2O_3 /Al composites with face-centered-tetragonal symmetry are compared with previous interpenetrating Al_2O_3 /Al composites with simple-tetragonal symmetry.

© 2009 Elsevier B.V. All rights reserved.

1. Introduction

Unlike many metal matrix composites (MMCs), which consist of discrete isolated fibers or particles within a metal matrix, ceramic-metal interpenetrating phase composites (IPCs) consist of two co-continuous and percolating ceramic and metal phases. IPCs have been shown to be advantageous over traditional MMCs [1–3] and show higher toughness than pure ceramics, as exemplified by cermets (e.g., WC–Co) with high-metal content [4–7]. Many processes exist to create light-weight Al_2O_3 –Al IPCs, e.g., infiltration of porous Al_2O_3 preforms [2,8–11], reactive metal penetration [12,13], and displacement reactions [3,14]. Unlike the latter composites where both phases are randomly distributed in space, Al_2O_3 –Al IPCs with periodic three-dimensional (3D) architectures can be produced by liquid-metal infiltration of 3D periodic ceramic preforms created by direct-ink writing, e.g., by using robocasting which has the capability to create structures with spanning (unsupported) features [15,16].

In a recent publication [17], we used synchrotron X-ray diffraction to measure internal strains developed during compressive deformation of interpenetrating Al_2O_3 –Al IPCs where the 3D periodic ceramic preform has simple-tetragonal (ST) symmetry. The extent of load transfer between the metal and ceramic phases was

examined and simple analytical predictions based on the rule-of-mixtures model were found to be in general agreement with the experimental data. Here, we extend this study to Al_2O_3 –Al IPCs where the 3D periodic ceramic preform exhibits face-centered-tetragonal (FCT) symmetry, to explore the effects of ceramic preform geometry on the mechanical properties and load transfer within these composites.

Another goal of the present study is to image the damage within these IPC composites. Due to the spatial coherency of x-ray beams from third generation synchrotron radiation sources, radiographic phase contrast imaging can obtain resolutions near 1 μm [18–20]. Phase contrast micro-radiography and high resolution micro-tomography have been used to nondestructively investigate many materials, especially within the field of biology and medicine [21–25], and specifically to study damage evolution in metal matrix composites (e.g., Al–SiC_{p/f} [18], Al–SiC_f [3], Al–SiC_p [26,27], Ti–SiC_f [28–31]). Here, we report on FCT symmetry preforms and the resulting infiltrated IPCs examined before and after compressive deformation by phase-contrast, edge-enhanced synchrotron X-ray imaging to examine their fracture modes.

2. Experimental procedures

2.1. Materials

Similar to 3D ceramic preforms with simple-tetragonal (ST) symmetry described in Ref. [17], ceramic preforms with a

* Corresponding author.

E-mail address: marcus.young@rub.de (M.L. Young).

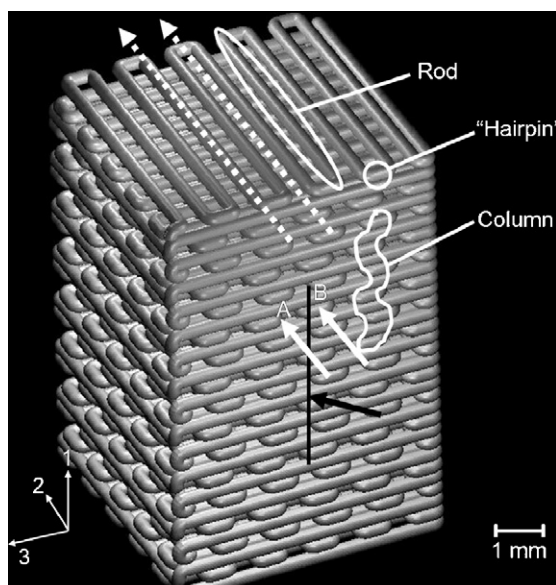


Fig. 1. Idealized 3D schematics of ceramic preform with face-centered-tetragonal symmetry. The metal phase (not shown) fills the space between the ceramic rods (diameter $\sim 250 \mu\text{m}$) and forms a skin ($\sim 100 \mu\text{m}$ deep) around the preform. The black arrow forming a 22° angle with the face corresponds to the beam used for 3 mm measurements, with the area rastered shown as the black line. The two white arrows perpendicular to the face show the X-ray beam ($150 \mu\text{m} \times 150 \mu\text{m}$) for spatially resolved measurements at positions (A) and (B). The corresponding beam path is illustrated with dashed line at the top of the preform, showing that position (A) samples a ceramic rod (consisting of both column and span regions) while position (B) samples a single ceramic hairpin (as well as metal).

regular $0/90^\circ$ architecture were produced by direct-write assembly of a colloidal gel-based Al_2O_3 ink (with 5 vol.% ZrO_2 as a sintering aid). Fig. 1 shows an idealized 3D schematic of a sintered ceramic preform with face-centered-tetragonal (FCT) symmetry. These preforms were created by using a four-layer repeat pattern, where the third and fourth layers are identical to the first two layers, but are shifted over by one half period. After fabrication, the processing of the FCT symmetry preforms was identical to that of ST symmetry preforms in Ref. [17], resulting in a final rod diameter of approximately $250 \mu\text{m}$ in the densified structures with nominal preform dimensions of $5 \text{ mm} \times 5 \text{ mm} \times 10 \text{ mm}$.

Sintered ceramic preforms were gas-pressure, liquid-metal infiltrated with either 99.99% pure aluminum or Al 7075 alloy (Al–5.6Zn–2.5Mg–1.6Cu–0.23Cr, in wt.%) as described in detail in Ref. [17]. The composites were machined into cuboids with two approximate dimensions ($4.5 \text{ mm} \times 4.5 \text{ mm} \times 9.9 \text{ mm}$ and $5.2 \text{ mm} \times 5.2 \text{ mm} \times 9.9 \text{ mm}$). In the case of the smaller specimens, all excess aluminum was machined from the exterior, leaving the edges of the ceramic preform exposed. By contrast, the larger specimens were machined in such a way to retain a $\sim 0.5 \text{ mm}$ thick metal outer layer around the ceramic preform. The pure aluminum matrix composites were annealed for 2 h at 350°C and air cooled. The Al 7075 alloy matrix composites were homogenized for 1 h at 490°C , water quenched, aged for 24 h at 120°C , and then water quenched again, corresponding to a T6 heat-treatment.

2.2. Synchrotron X-ray imaging measurements

Ceramic preforms and pre- and post-compression composites of both symmetries were imaged at the 1-ID beam line of the Advanced Photon Source (Argonne National Laboratory, IL). The composites were positioned with their vertical faces perpendicular/parallel ($0/90^\circ$) to the beam. Radiographic images were collected using a monochromatic 81 keV ($\lambda = 0.015 \text{ nm}$) X-ray beam

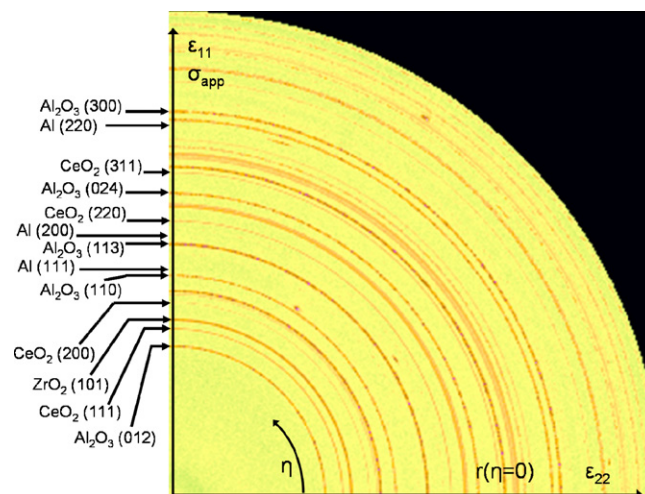


Fig. 2. Representative X-ray diffraction pattern (quarter of image plate) of composite F-7075 for an average bulk measurement. All full diffraction rings were identified and assigned to CeO_2 , Al_2O_3 or ZrO_2 , while the Al rings were spotty and incomplete. For clarity, only some of the rings are labeled here. Sample-to-camera distance for this diffraction pattern was 1.220 m. Strains e_{11} and e_{22} are measured in the direction shown.

with a square cross-sectional field of view of $2 \text{ mm} \times 2 \text{ mm}$. Images were recorded using a CCD camera, positioned far enough (about 0.7 m) from the sample to allow for phase propagation (phase-enhanced imaging) [18].

2.3. Synchrotron X-ray diffraction measurements

As described in detail in Ref. [17], high-energy X-ray diffraction measurements were collected at the 1-ID and 11-ID beam lines of the Advanced Photon Source using a monochromatic 81 keV ($\lambda = 0.015 \text{ nm}$) or 93 keV ($\lambda = 0.013 \text{ nm}$) X-ray beam for 60 s. The incident X-ray beam in diffraction mode generally had a square cross-section with a size of $150 \mu\text{m} \times 150 \mu\text{m}$. Complete Debye–Scherrer diffraction rings originating from the diffraction volumes were recorded using an image plate (MAR345) as described in Ref. [17]. The sample-to-camera distance was 1.220 or 2.100 m. A typical diffraction pattern for the former sample-to-camera distance is shown in Fig. 2. As described in Ref. [17], additional calibration diffraction cones are produced from a paste composed of vacuum grease and pure ceria (CeO_2) powder. All phases present are fine grained and polycrystalline (leading to very fine diffraction rings) except for the Al phase, which is very coarse grained (due to the casting method) and thus produces spotty diffraction rings, which cannot be used for strain measurements. As described in detail in Ref. [32], the programs FIT2D [33,34] and MATLAB [35] are used to determine lattice strains from distortions of the diffraction rings of the Al_2O_3 and ZrO_2 phases.

The two larger composites with Al outer layer (labeled F-Al for pure Al matrix and F-7075 for the alloy matrix, where “F” stands for “face-centered-tetragonal”) were subjected to uniaxial compressive loading and unloading with $\sim 15 \text{ MPa}$ stress increments. The third, smaller specimen without Al outer layer (labeled F-Al(R), where “R” stands for “spatially resolved”) was used to carry out spatially resolved measurements. These *in situ* uniaxial compressive experiments were performed using a small, custom-built, screw-driven loading system. The general setup for these experiments has been described previously [17,32,36–43]. As described in detail in Ref. [17], spatially resolved and average bulk synchrotron X-ray diffraction measurements were collected at each stress level. For spatially resolved measurements, two positions (A and B) are studied, as shown in Figs. 1 and 3: (i) along a horizontal ceramic rod (A)

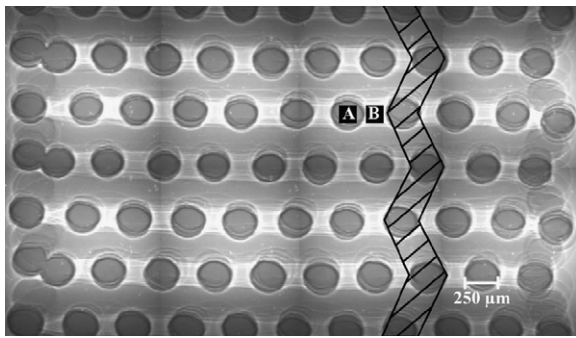


Fig. 3. X-ray phase-enhanced radiograph of middle section of ceramic preform with face-centered-tetragonal symmetry (projection perpendicular to the 3 direction). The rod diameter is about 250 μm . The black boxes indicate beam size (150 μm \times 150 μm) and position of spatially resolved measurements for positions (A) along a ceramic rod and (B) between two rods, sampling metal phase and a single ceramic “hairpin” connecting two adjacent rods at the edge of the composite. A column, connected with 6 horizontal strut series, is highlighted.

and (ii) between ceramic rods, along a matrix horizontal channel (B).

3. Results

3.1. Microstructure

As for the IPCs with ST symmetry studied in Ref. [17], the Al_2O_3 volume fractions of the three present composites with FCT symmetry range from 50 to 56%, as determined from density measurements by He pycnometry. Like the ST symmetry preforms in Ref. [17], good alignment of the layers and good spacing between horizontal columns, except near the sample edges, are observed in FCT symmetry preforms, as shown in the X-ray phase-enhanced radiograph in Fig. 3.

3.2. Phase-contrast, edge-enhanced imaging

Fig. 4A and B shows X-ray phase-enhanced images of a FCT symmetry composite F-Al(R) after compression testing up to failure, which occurred at 250 MPa; this value is much lower than measured previously on similar ST symmetry composites (700 MPa [16] and up to 330 MPa without failure [17]). Although not shown here, X-ray phase-enhanced images of ST symmetry composites were also collected after compression testing. No large-scale fracture occurred in ST symmetry composites; however, some microscopic fracture events were observed within the ceramic phase.

During compression testing, ST-symmetry and FCT-symmetry composites experience different localized loading configurations at the strut and column level, due to differing geometries. For ST symmetry composites, the columns experience near uniaxial compression while the horizontal struts (spans) experience a more complex state of stress, dictated by load transfer from the surrounding ceramic columns and metallic matrix. These spans tend to fracture with the plane of fracture parallel or nearly parallel to the loading direction (1-axis). For the FCT symmetry composites studied here, spans experience loading from the surrounding ceramic phase similar to 3-point bend testing as observed in the close-up image in Fig. 4B and, like the ST symmetry composites, fracture occurs typically with the plane of fracture parallel or nearly parallel to the loading direction (1-axis).

Fracture of the ceramic preform within the composite can be seen as a combination of vertical and off-axis cracks occurring along a span between two horizontal rods for the FCT symmetry composites. The location of the cracks is predominately near the edges of the composite where Al is less constrained leading to Al_2O_3 damage

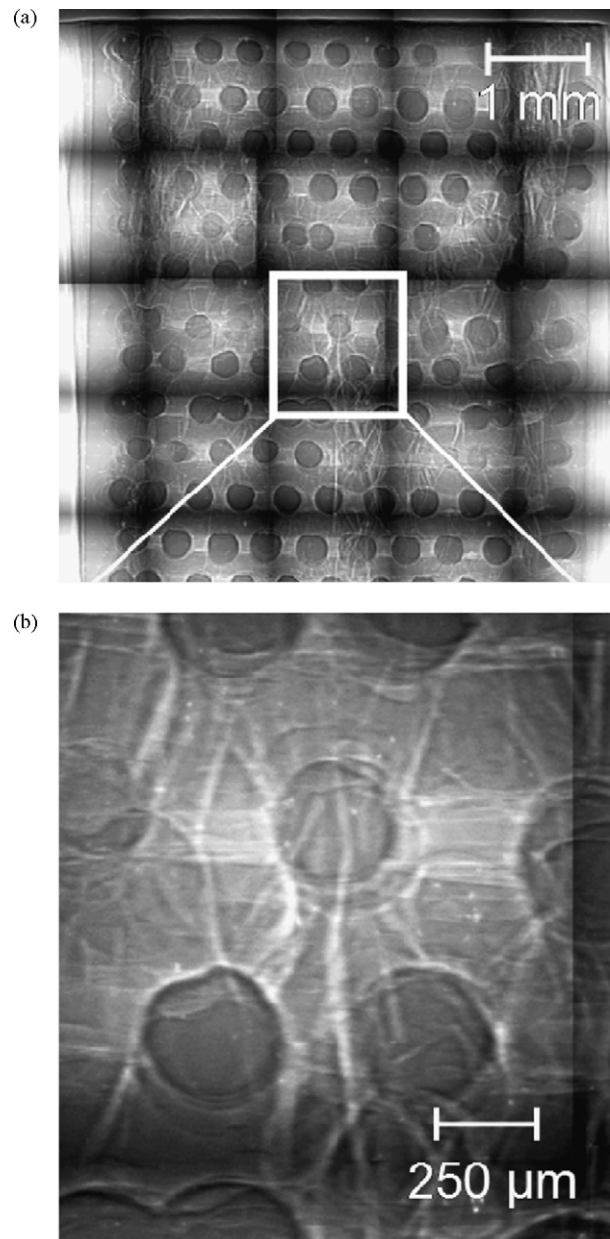


Fig. 4. X-ray phase-contrast, edge-enhanced images of half of an entire composite with FCT symmetry (F-7075) illustrating (A) large-scale fracture behavior and (B) a detailed view of microscopic fracture behavior. The complete image of the composite is a mosaic of individual radiographic images ($\sim(1\text{--}2)$ mm \times $(1\text{--}2)$ mm). The white box shows a detailed view of X-ray phase-contrast, edge-enhanced images illustrating typical microscopic crack behavior for FCT symmetry composites. The vertical and nearly white vertical lines correspond to fractures within the ceramic phase.

and lateral displacement, visible as column fragments jutting out of the sample's lateral sides as illustrated in the larger image (Fig. 4A). Although presumably cracking in the Al metal phase occurs, it was not observed in the X-ray radiographic images.

3.3. Synchrotron diffraction strain measurements

3.3.1. Commonality among samples

Commonalities among three ST symmetry Al– Al_2O_3 composites (S-Al, S-7075, and S-Al(R)) have been described in Ref. [17] and are present as well among the three FCT symmetry Al– Al_2O_3 composites presented here. For all three samples, plots of the applied stress vs. average elastic lattice strain for the Al_2O_3 (1 1 3) reflec-

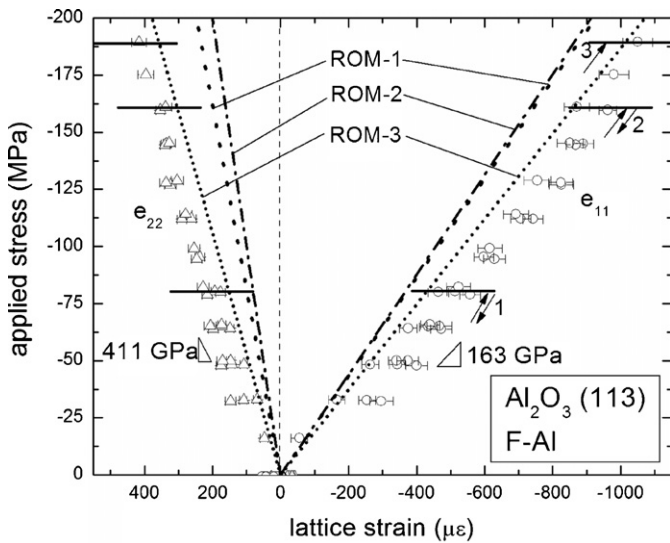


Fig. 5. Applied stress as a function of elastic lattice strain (bulk average values, e_{11} parallel and e_{22} perpendicular to the applied stress) for F-Al composite using Al_2O_3 (1 1 3) reflection upon multiple loading-unloading cycles (marked 1–3). Failure occurred upon loading of the third cycle. Slopes are best fit values for all experimental data. The slopes for the Al_2O_3 (1 1 3) reflection were determined as best fit of all experimental data. Three rule-of-mixture models (ROM-1, ROM-2 and ROM-3) are also plotted for the 2 direction.

tion are shown in Figs. 5–7. Several other Al_2O_3 reflections were used to calculate lattice strains, but are not shown here, since the above two reflections are representative of the bulk given the nearly isotropic behavior, as discussed in detail in Ref. [17]. The ZrO_2 phase behavior follows that of the Al_2O_3 phase, the only difference being that the slope for the ZrO_2 phase is lower than that for the Al_2O_3 phase, as expected theoretically from the respective moduli for pure Al_2O_3 ($E_{\text{Al}_2\text{O}_3} = 380 \text{ GPa}$ [44]) and partially stabilized ZrO_2 ($E_{\text{ZrO}_2} = 205 \text{ GPa}$ [44]) as also discussed in detail in Ref. [17]. In Figs. 5–7, the lattice strains for the Al_2O_3 phase become more compressive (negative) in the loading direction (e_{11}) and more tensile (positive) in the transverse direction (e_{22}), as expected from the uniaxial compressive load applied to the sample in the 1 direction (Fig. 1). Varying amounts of residual strains at zero applied stress

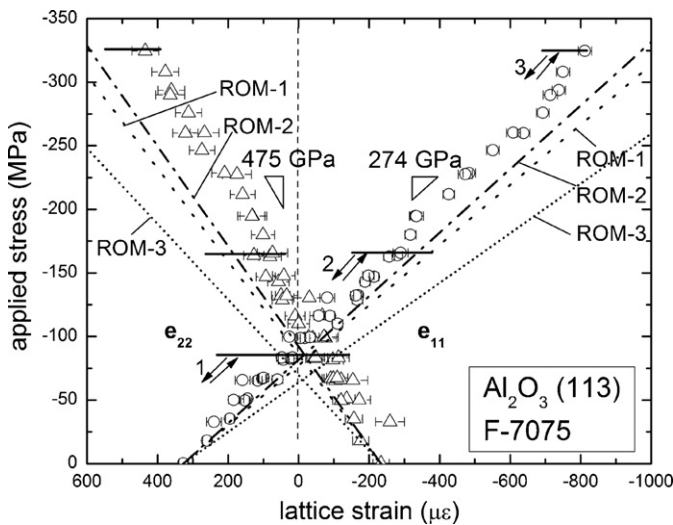


Fig. 6. Applied stress as a function of elastic lattice strain (bulk average values, e_{11} parallel and e_{22} perpendicular to the applied stress) for F-7075 composite using the Al_2O_3 (1 1 3) reflection upon multiple loading-unloading cycles (marked 1–3). Slopes are best fit values for all experimental data. Three rule-of-mixture models (ROM-1, ROM-2 and ROM-3) are also plotted for the 2 direction.

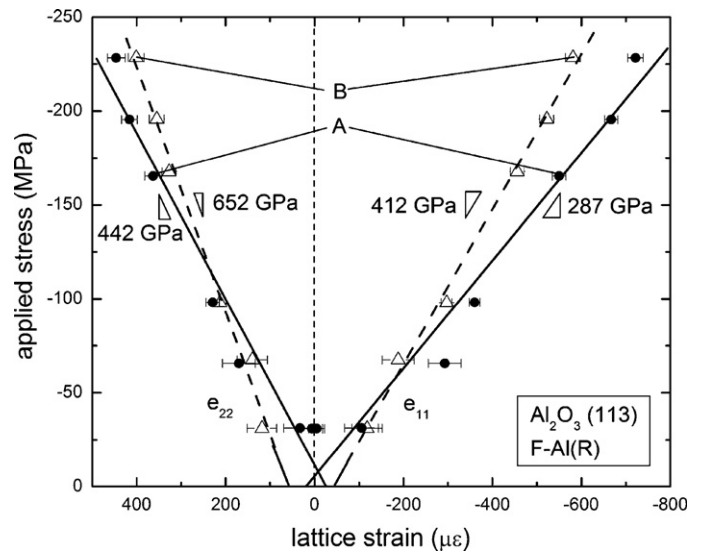


Fig. 7. Applied stress as a function of elastic lattice strain (e_{11} parallel and e_{22} perpendicular to the applied stress) for a F-Al(R) using the Al_2O_3 (1 1 3) reflection upon loading. Spatially resolved measurements are along a ceramic rod (A: closed circles) and along a metallic channel and a single “hairpin” connecting two rods (B: open triangles). The lines are a linear fit to the loading data.

are observed, and they are invariably tensile in the loading direction and compressive in the transverse direction. Finally, no large-scale damage can be deduced from the internal lattice strain measurements during cyclic loading (i.e., departure from a purely linear behavior in Figs. 5–7), despite some damage visible on the surface of composites F-Al and F-Al(R). The following sections discuss in detail the behavior of the various composites during compression testing and cyclic loading.

3.3.2. Bulk diffraction strain measurements

Sample F-Al with a density of $3.39 \pm 0.005 \text{ g/cm}^3$ (corresponding to a pure aluminum volume fraction of $50.16 \pm 0.35\%$) and with dimensions $5.26 \text{ mm} \times 5.31 \text{ mm} \times 9.85 \text{ mm}$ was cyclically tested to failure as follows: $0 \rightarrow 80 \rightarrow 33 \text{ MPa}$, $33 \rightarrow 160 \rightarrow 32 \text{ MPa}$, and $32 \rightarrow 190 \text{ MPa}$, where failure occurred. As illustrated in Fig. 5, near-zero residual strains at zero applied stress are tensile in the loading direction ($13 \pm 25 \mu\epsilon$) and compressive in the transverse direction ($-31 \pm 12 \mu\epsilon$) for the Al_2O_3 (1 1 3) reflection, which is similar to the results for ST symmetry composites with pure aluminum [17]. Upon cyclic elastic loading, the apparent elastic moduli for the Al_2O_3 phase (corresponding to the experimentally measured slopes of the stress–elastic strain curves of the Al_2O_3 (1 1 3) reinforcement) are 163 GPa in the loading direction and 411 GPa in the transverse direction, and remain near constant as the maximum stress value of the cycle increases.

Sample F-7075 with a density of $3.47 \pm 0.004 \text{ g/cm}^3$ (corresponding to a 7075 alloy volume fraction of $43.88 \pm 0.35\%$) and dimensions $5.22 \text{ mm} \times 5.28 \text{ mm} \times 10.06 \text{ mm}$, was cyclically tested without failure as follows: $0 \rightarrow 85 \rightarrow 50 \text{ MPa}$, $50 \rightarrow 165 \rightarrow 50 \text{ MPa}$, and $50 \rightarrow 325 \rightarrow 0 \text{ MPa}$. As illustrated in Fig. 6 and similar to results from bulk measurements in ST symmetry composites with Al 7075 alloy [17], residual strains at zero applied stress are tensile in the loading direction ($327 \pm 12 \mu\epsilon$) and compressive in the transverse direction ($-234 \pm 23 \mu\epsilon$) for the Al_2O_3 (1 1 3) reflection. Upon cyclic elastic loading, the apparent elastic moduli of the Al_2O_3 (1 1 3) reinforcement are 274 GPa in the loading direction and 475 GPa in the transverse direction.

3.3.3. Spatially resolved diffraction strain measurements

Sample F-Al(R) with a density of $3.42 \pm 0.03 \text{ g/cm}^3$, corresponding to a pure aluminum volume fraction of $48.04 \pm 1.97\%$ and dimensions $4.49 \text{ mm} \times 4.52 \text{ mm} \times 9.82 \text{ mm}$, was compression tested to failure as follows: $31 \rightarrow 68 \rightarrow 98 \rightarrow 134 \rightarrow 167 \rightarrow 196 \rightarrow 228 \rightarrow 263 \text{ MPa}$, where failure occurred. At each load increment of $\sim 30 \text{ MPa}$, spatially resolved measurements were taken in two positions along an horizontal ceramic rod (marked A in Figs. 1 and 3) and at a ceramic “hairpin” connecting two rods (B in Figs. 1 and 3). The resulting applied stress plotted as a function of the average elastic lattice strain curve for the Al_2O_3 (1 1 3) reflection is shown in Fig. 7.

Similar to bulk measurements and to the results for the spatially resolved measurements for an ST symmetry composite [17], residual strains are present for both positions A and B. As described in Ref. [17] for spatially resolved measurements of ST symmetry composites, since no values are collected at zero applied load, the values for residual strains are extrapolated based on the slope of the best linear fit of the low-stress region (0–31 MPa). For position A (along a rod), the residual strains are tensile in the loading direction ($20 \mu\epsilon$) and compressive in the transverse direction ($-25 \mu\epsilon$). For position B (“hairpin” only), the residual strains are compressive in the loading direction ($-45 \mu\epsilon$) and tensile in the transverse direction ($60 \mu\epsilon$). Similar to the bulk average measurements, load transfer is evident from the metal phase to the ceramic phase. In this case, however, load transfer varies with position. In the first position B, where only an alumina “hairpin” (i.e., a single horizontal strut) is examined, the apparent elastic moduli (412 and 652 GPa in the loading and transverse directions, respectively) are lower than in the second position A, along a row of struts and columns, where the apparent elastic moduli are 287 and 442 GPa, respectively.

4. Discussion

4.1. Phase-contrast, edge-enhanced imaging

As seen in post-compression radiographic images for F-Al(R) in Fig. 4A and B, fracture occurs predominantly across spans with the plane of fracture parallel or nearly parallel to the loading direction (1-axis) for FCT symmetry composites. Cracks seem to start at the contact point between a column and a span (which are perpendicular to each other) and propagate across one of the spans to another underlying column (which is also perpendicular to the fractured span). As the composites are loaded in compression, the columns experience a compressive force, while the spans experience both a compressive force in the direction of loading and, in some cases, a tensile force acting to prevent buckling of the columns. This fracture mechanism has been observed previously in periodic mullite structures [45] and in periodic alumina structures [16] without a metallic matrix. As suggested in Ref. [16], fracture is initiated by defects at the junctions between the columns and spans. On a large-scale, multiple fracture events like the ones described here occur from the corners to the center of the composite, leading to macroscopic failure of the composite as observed in Fig. 4A.

4.2. Bulk diffraction strain measurements

Similar to results for IPCs with ST symmetry [17], low residual strains are observed in sample F-Al, while larger residual strains are observed in sample F-7075. These residual strains are due to the different heat treatments (i.e., F-Al was air cooled resulting in much lower residual strains than those observed in the F-7075, where the sample was water quenched according to the T6 heat-treatment) and are discussed in detail in Ref. [17], where similar residual strains were observed in IPCs with ST symmetry and similar processing methods. For bulk lattice strain measurements, the

apparent elastic moduli of the average bulk Al_2O_3 (1 1 3) reinforcement phase for F-Al (163 GPa) and F-7075 composites (274 GPa) are respectively 45 and 75% lower than the Young's modulus for the bulk Al_2O_3 –5% ZrO_2 phase (calculated as 365 GPa in Ref. [17] from the Young's moduli of pure Al_2O_3 , $E_{\text{Al}_2\text{O}_3} = 380 \text{ GPa}$ [44], and partially stabilized ZrO_2 , $E_{\text{ZrO}_2} = 205 \text{ GPa}$ [44]). This decrease is a result of load transfer from the less stiff metal phase to the stiffer ceramic phase, which is discussed in detail in Ref. [17]. Besides the primary load transfer from the metal phase to the ceramic phase, there is also a secondary, though much less significant, load transfer within the ceramic phase occurring from the ZrO_2 phase to the Al_2O_3 phase [17].

The apparent elastic moduli of sample F-7075 exhibited, within experimental error, identical behavior to that of S-7075 in Ref. [17] and will not be discussed in further detail. The apparent elastic modulus of sample F-Al (163 GPa with 49.8 vol.% Al_2O_3) is a factor of 0.67–0.77 lower than values here (274 GPa with 56.1 vol.% Al_2O_3 for F-7075) and of those previously reported (242 GPa for S-Al with 50.0 vol.% Al_2O_3 and 263 GPa for S-7075 with 56.7 vol.% Al_2O_3 [17]) for the Al_2O_3 (1 1 3) reflection. It is unclear why this sample exhibits a significantly lower apparent elastic modulus and this cannot be explained on the basis of the volume fraction of Al_2O_3 . It is possible that this particular FCT preform was damaged after sintering and before metal infiltration, thus making the overall composite weaker due to pre-cracking in the ceramic phase before loading. It is also possible that the preform was not as completely sintered as those of other samples, such that small gaps between the overlapping rods may be present, a processing defect sometimes observed. Unlike other composites presented here and in Ref. [17] where the value of the apparent elastic modulus remained constant within experimental error throughout cyclic loading, sample F-Al shows an increasing value for the apparent elastic modulus as a function of loading (Fig. 5). In the first cycle, the apparent elastic moduli of the Al_2O_3 (1 1 3) reinforcement are 154 GPa in the loading direction and 367 GPa in the transverse direction. In the second cycle, these moduli are 171 and 477 GPa, respectively. In the last cycle before failure, they are 210 and 593 GPa, respectively. This increase in apparent stiffness upon cyclic loading suggests that the ceramic phase supports less stress as the composite becomes more deformed, indicative of damage. Unlike composites presented in Ref. [17] and here for F-7075 (with a ratio of the slopes equal to 0.57), the average stress state of the Al_2O_3 phase is close to uniaxial compressive with the ratio of the slopes (apparent stiffness in loading and transverse directions) equal to 0.39, which is close to the Poisson's ratios value of 0.33 [46] for pure Al_2O_3 .

Overall, the ST symmetry composites from Ref. [17] have higher strength than the FCT symmetry composites studied here: none of the former ST composites failed at the maximum load, whereas only one of the FCT symmetry composites did not fail and this sample (F-7075) was alloyed with Al 7075 which is stiffer and stronger than pure Al. This dichotomy is probably due to the improved strength of the ST vertical load-bearing columns as compared the zigzagging FCT columns in which tensile stress components are more likely to develop, leading to earlier failure (since Al_2O_3 is significantly weaker in tension than in compression [37]). However, the failure behavior may also be controlled by defects within the alumina preforms, e.g., misalignment of rods near the sample edges.

4.3. Spatially resolved diffraction strain measurements

Sample F-Al(R) shows spatially resolved strain results which are similar to those of sample S-Al(R), which is discussed in detail in Ref. [17]. Although measurable residual strains (~ 20 – $70 \mu\epsilon$) are present, they are relatively small as compared to the fracture strains of alumina. As for ST symmetry composites [17], load transfer varies with position (Fig. 7). Position (A) exhibits a lower apparent elas-

tic modulus and, therefore, a larger extent of load transfer than position (B), where positions (A) and (B) correspond respectively to a horizontal rod and a single “hairpin” connecting two rods.

Upon loading, position A (along a rod) experiences a larger increase in compressive strain and at a maximum load of 228 MPa, this compressive strain increases by approximately 124% in the loading direction and 111% in the transverse direction more than in position B (the “hairpin” between two columns). This behavior is similar to fiber composites where longitudinal fibers are significantly stronger than transverse fibers under compressive loading. However, in this case, the situation is more complicated since horizontal rods include a combination of stacks of columns (longitudinal fibers) and struts (transverse fibers) and position (B) only includes the “hairpin” (i.e., a single strut or a single transverse fiber) between two rods.

Position A experiences both compressive and tensile stresses during compressive loading. The columns experience compression in the 1 direction, while the struts experience both compression from loading and tension from the nearby columns in compression. Similarly, position B (the “hairpin” between two columns), besides experiencing a compressive stress in the 1 direction, is also experiencing a tensile stress in the 3 direction from the nearby columns in compression (i.e., tension on the strut resulting from these columns buckling away from each other thus pulling on the connecting rod). Since there is more Al metal in this region, there should be less strain on B due to load transfer from the Al metal phase to the ceramic phase. As this region is being compressed, the deforming Al metal is expected to transfer stresses to the neighboring columns, thus lowering the overall stress experienced by the strut. As a result, position B experiences slightly lower compressive stresses and strains, as measured in the 1 direction, than position A along a column.

4.4. Load transfer modeling by rule-of-mixture calculations

As described in detail in Ref. [17], three models based on rule-of-mixtures [47] (labeled ROM-1, ROM-2, and ROM-3) predict apparent elastic moduli for the Al_2O_3 phase within the error of experimental data. As illustrated in Figs. 5 and 6, respectively, the results from these ROM models are compared with bulk measurements from Al_2O_3 (1 1 3) for a FCT symmetry composite with 99.99% pure Al (F-Al) and a FCT symmetry composite with Al-7075 alloy (F-7075) in the longitudinal (e_{11}) and transverse directions (e_{22}). For each set of data, the appropriate volume fractions of Al_2O_3 (49.8% for F-Al and 56.1% for F-7075) were used for the models.

An in-depth discussion of the three ROM models is given in Ref. [17]. As discussed earlier, F-Al exhibits a significantly lower apparent elastic modulus (Fig. 5) than any other ST or FCT sample, which results in over-prediction of the apparent elastic moduli of the ROM models and, therefore, will not be discussed further. Examining F-7075 (Fig. 6) reveals that the ROM-1 and ROM-2 models predict the longitudinal strains much better than the ROM-3 model, as was also observed in ST symmetry composites [17]. However, the ROM-1 and ROM-2 models predict reasonably well the transverse strains in the FCT composites as compared to the ROM-3 model. All three ROM models over-predict the transverse strains for FCT symmetry composites, unlike for the ST symmetry composites where the ROM models under-predict the transverse strains [17]. Given the simplicity of these ROM models and the limitations associated with their use [17], they provide reasonable approximation apparent elastic moduli of the experimental data for both FCT and ST symmetry composites.

5. Conclusions

Synchrotron X-ray radiation was used to investigate interpenetrating Al_2O_3 -Al composites produced by liquid-metal infiltration

of 3D periodic Al_2O_3 preforms with face-centered-tetragonal (FCT) symmetry fabricated by direct-write assembly. X-ray phase-enhanced images were collected from ceramic preforms and pre- and post-compression tested Al_2O_3 -Al composites, providing information on localized ceramic damage in the composite. X-ray diffraction was used to measure, before compression testing, low residual strains due to thermal mismatch. During uniaxial compression, the elastic strain in the ceramic phase increases linearly with increasing applied stress and the ceramic phase becomes increasingly damaged. Simple rule-of-mixture models provide reasonable approximations of the strains in the ceramic phase. Spatially resolved measurements show that less overall strain is observed in the ceramic “hairpins” (perpendicular to the applied load) than in the “columns” parallel to the applied load, as expected. Comparisons are made with a previous study where similar Al_2O_3 -Al composites with simple-tetragonal (ST) symmetry were studied.

Acknowledgments

The authors thank Drs. Ulrich Lienert, Kamel Fezzaa, and Wah-Keat Lee at the APS (SRI-CAT) and Dr. Mark Beno and Chuck Kurtz at the APS (BESSRC-CAT) at ANL for experimental assistance. Dr. Jennifer A. Lewis and Ranjeet Rao acknowledge funding provided by NSF Grant # (DMR01-17792). The robocasting apparatus used in this work was designed and built by J. Cesarano, and customized software for 3D fabrication was developed by J.E. Smay. Dr. Deming Shu at the APS built the compression rig. Use of the APS was supported by the U.S. Department of Energy, Office of Science, Office of Basic Energy Science, under contract number DE-AC02-06CH11357.

References

- [1] L.D. Wegner, L.J. Gibson, *International Journal of Mechanical Sciences* 42 (2000) 925–942.
- [2] H. Prielipp, M. Knechtel, N. Claussen, S.K. Streiffer, H. Müllejans, M. Ruhle, J. Rodel, *Materials Science and Engineering A* 197 (1995) 19–30.
- [3] D.K. Balch, T.J. Fitzgerald, V.J. Michaud, A. Mortensen, Y.L. Shen, S. Suresh, *Metallurgical and Materials Transactions A* 27 (1996) 3700–3717.
- [4] H.C. Lee, J. Gurland, *Materials Science and Engineering A* 33 (1978) 125–133.
- [5] V.K. Sarin, *Cemented carbide cutting tools*, in: G.Y. Chin (Ed.), *Advances in Powder Technology, Materials Science Seminar*, ASM, Louisville, KY, 1981, pp. 253–288.
- [6] L.S. Sigl, H.E. Exner, *Metallurgical, Materials Transactions A-Physical Metallurgy and Materials Science* 18 (1987) 1299–1308.
- [7] J.R. Tinklepaugh, W.B. Crandall, *Cermets*, Reinhold Publishing Corporation, New York, 1960.
- [8] M. Kouzeli, D.C. Dunand, *Metallurgical and Materials Transactions A-Physical Metallurgy and Materials Science* 35A (2004) 287–292.
- [9] S. Skirl, M. Hoffman, K. Bowman, S. Wiederhorn, J. Rodel, *Acta Materialia* 46 (1998) 2493–2499.
- [10] A. Zimmermann, M. Hoffman, T. Emmel, D. Gross, J. Rodel, *Acta Materialia* 49 (2001) 3177–3187.
- [11] S. Roy, J. Gibmeier, A. Wanner, *Advanced Engineering Materials* 11 (2009) 471–477.
- [12] K.G. Ewsuk, S.J. Glass, R.E. Loehman, A.P. Tomsia, W.G. Fahrenholtz, *Metallurgical and Materials Transactions A-Physical Metallurgy and Materials Science* 27 (1996) 2122–2129.
- [13] R.E. Loehman, K.G. Ewsuk, A.P. Tomsia, *Journal of the American Ceramic Society* 79 (1996) 27–32.
- [14] M.C. Breslin, J. Ringnalda, L. Xu, M. Fuller, J. Seeger, G.S. Daehn, T. Otani, H.L. Fraser, *Materials Science and Engineering A* 195 (1995) 113–119.
- [15] J. Cesarano, P. Calvert, US Patent 6,027,326 (2000).
- [16] C. San Marchi, M. Kouzeli, R. Rao, J.A. Lewis, D.C. Dunand, *Scripta Materialia* 49 (2003) 861–866.
- [17] M.L. Young, R. Rao, J.D. Almer, D.R. Haeflner, J.A. Lewis, D.C. Dunand, *Acta Materialia* 57 (2009) 2362–2375.
- [18] P. Cloetens, R. Barrett, J. Baruchel, J.P. Guigay, M. Schlenker, *Journal of Physics D: Applied Physics* 29 (1996) 133–146.
- [19] C. Raven, A. Snigireva, I. Snigireva, P. Spanne, A. Souvorov, V. Kohn, *Applied Physics Letters* 69 (1996) 1826–1828.
- [20] K. Janssens, G. Vittiglio, I. Deraedt, A. Aerts, B. Vekemans, L. Vincze, F. Wei, I. Deryck, O. Schalm, F. Adams, A. Rindby, A. Knochel, A. Simionovici, A. Snigireva, *X-ray Spectrometry* 29 (2000) 73–91.
- [21] S.R. Stock, *International Materials Reviews* 44 (1999) 141–164.
- [22] S.R. Stock, K. Ignatiev, T. Dahl, J. Barss, K. Fezzaa, A. Veis, W.K. Lee, F. De Carlo, *Journal of Synchrotron Radiation* 10 (2003) 393–397.

- [23] S.R. Stock, W.K. Lee, K. Fezzaa, J. Barss, T. Dahl, A. Veis, *Journal of Bone and Mineral Research* 16 (2001) S443–S1443.
- [24] M.W. Westneat, O. Betz, R. Blob, K. Fezzaa, J. Cooper, W.K. Lee, *American Zoologist* 41 (2001) 1623–1624.
- [25] M.W. Westneat, O. Betz, R.W. Blob, K. Fezzaa, W.J. Cooper, W.K. Lee, *Science* 299 (2003) 558–560.
- [26] J.-Y. Buffiere, E. Maire, P. Cloetens, G. Lormand, R. Fougères, *Acta Materialia* 47 (1999) 1613–1625.
- [27] J.-Y. Buffiere, E. Maire, C. Verdu, P. Cloetens, M. Pateyron, G. Peix, J. Baruchel, *Materials Science and Engineering A* 234–236 (1997) 633–635.
- [28] M. Preuss, P.J. Withers, E. Maire, J.-Y. Buffiere, *Acta Materialia* 50 (2002) 3177–3192.
- [29] S. MacDonald, M. Preuss, E. Maire, J.-Y. Buffiere, P.M. Mummery, P.J. Withers, *Journal of Microscopy* 209 (2003) 102–112.
- [30] E. Maire, R.A. Owen, J.-Y. Buffiere, P.J. Withers, *Acta Materialia* 49 (2001) 153–163.
- [31] R. Sinclair, M. Preuss, E. Maire, J.-Y. Buffiere, P. Bowen, P.J. Withers, *Acta Materialia* 52 (2004) 1423–1438.
- [32] M.L. Young, J.D. Almer, M.R. Daymond, D.R. Haefner, D.C. Dunand, *Acta Materialia* 55 (2007) 1999–2011.
- [33] A.P. Hammersley, ESRF97HA02T, FIT2D: an introduction and overview, in: ESRF Internal Report, 1997.
- [34] A.P. Hammersley, ESRF98HA01T, FIT2D V9.129 reference manual V3.1, in: ESRF Internal Report, 1998.
- [35] M. MATLAB, in: p. Available from: <http://www.mathworks.com>.
- [36] A. Wanner, D.C. Dunand, *Metallurgical and Materials Transactions A-Physical Metallurgy and Materials Science* 31 (2000) 2949–2962.
- [37] M.L. Young, J.D. Almer, U. Lienert, D.R. Haefner, R. Rao, J.A. Lewis, D.C. Dunand, MS&T conference proceedings: affordable metal matrix composites for high performance applications II, in: A.B. Pandey, K.L. Kendig, J.J. Lewandowski, S.R. Shah (Eds.), *Materials Science and Technology*, TMS, Chicago, IL, 2003, pp. 225–233.
- [38] A. Wanner, D.C. Dunand, *Journal of Neutron Research* 10 (2002) 57.
- [39] D.K. Balch, D.C. Dunand, *Acta Materialia* 54 (2006) 1501–1511.
- [40] D.K. Balch, E. Ustundag, D.C. Dunand, *Journal of Non-Crystalline Solids* 317 (2003) 176–180.
- [41] D.K. Balch, E. Ustundag, D.C. Dunand, *Metallurgical and Materials Transactions A-Physical Metallurgy and Materials Science* 34A (2003) 1787–1797.
- [42] J.D. Almer, S.R. Stock, *Journal of Structural Biology* 152 (2005) 14–27.
- [43] D.R. Haefner, J.D. Almer, U. Lienert, *Materials Science and Engineering A* 399 (2005) 120–127.
- [44] *Engineering Materials Handbook: Ceramics and Glasses*, ASM Publication, 1991.
- [45] A. Hattiangadi, A. Bandyopadhyay, *Journal of American Ceramic Society* 83 (2000) 2730.
- [46] *Metals Handbook*, vol. 2, ASM Handbook Committee, American Society for Metals, Metals Park, OH, 1990.
- [47] T.H. Courtney, *Mechanical Behavior of Materials*, McGraw Hill, 2000.